

A systematic fitting scheme for caustic-crossing microlensing events

N.Kains^{1,2,*}, A. Cassan^{1,3}, K.Horne^{1,2}, M.D. Albrow^{1,4}, S. Dieters^{1,5},
P. Fouqué^{1,6}, J. Greenhill^{1,7}, A. Udalski^{8,9}, M. Zub^{1,3,†}, D.P. Bennett^{1,10},
M. Dominik^{2,‡}, J. Donatowicz^{1,11}, D. Kubas^{1,12}, Y. Tsapras^{1,13}, T. Anguita³,
V. Batista^{1,5}, J.-P. Beaulieu^{1,5}, S. Brilliant^{1,12}, M. Bode^{1,13}, D.M. Bramich^{1,14},
M. Burgdorf^{1,13}, J.A.R. Caldwell^{1,15}, K.H. Cook^{1,16}, Ch. Coutures^{1,17},
D. Dominis Prester^{1,18}, U.G. Jørgensen^{1,19}, S. Kane^{1,20}, J.B. Marquette^{1,5},
R. Martin^{1,21}, J. Menzies^{1,22}, K.R. Pollard^{1,4}, N. Rattenbury^{1,23}, K.C. Sahu^{1,24},
C. Snodgrass^{1,12}, I. Steele^{1,11}, C. Vinter^{1,19}, J. Wambsganss^{1,3}, A. Williams^{1,21},
M. Kubiak^{8,9}, G. Pietrzyński^{8,9,25}, I. Soszyński^{8,9}, O. Szewczyk^{8,9,25},
M.K. Szymański^{8,9}, K. Ulaczyk^{8,9} L.Wyrzykowski^{13,26}

¹ PLANET/RoboNet collaborations

² SUPA, School of Physics and Astronomy, University of St. Andrews, North Haugh, St Andrews, KY16 9SS, United Kingdom

³ Astronomisches Rechen-Institut (ARI), Zentrum für Astronomie (ZAH), Heidelberg University, Mönchhofstraße 12-14, 69120 Heidelberg, Germany

⁴ University of Canterbury, Department of Physics and Astronomy, Private Bag 4800, Christchurch, New Zealand

⁵ Institut d'Astrophysique de Paris, UMR7095 CNRS, Université Pierre & Marie Curie, 98bis Boulevard Arago, 75014 Paris, France

⁶ LATT, Université de Toulouse, CNRS, 14 avenue Edouard Belin, F-31400 Toulouse, France

⁷ School of Mathematics and Physics, University of Tasmania, Private Bag 37, Hobart, Tasmania 7001, Australia

Accepted ... Received ... ; in original form ...

ABSTRACT

We outline a method for fitting binary-lens caustic-crossing microlensing events based on the alternative model parameterisation proposed and detailed in Cassan (2008). As an illustration of our methodology, we present an analysis of OGLE-2007-BLG-472, a double-peaked Galactic microlensing event with a source crossing the whole caustic structure in less than three days. In order to identify all possible models we conduct an extensive search of the parameter space, followed by a refinement of the parameters with a Markov Chain-Monte Carlo algorithm. We find a number of low- χ^2 regions in the parameter space, which lead to several distinct competitive best models. We examine the parameters for each of them, and estimate their physical properties. We find that our fitting strategy locates several minima that are difficult to find with other modelling strategies and is therefore a more appropriate method to fit this type of events.

Key words: gravitational microlensing - data modelling - extrasolar planets - binary stars - robotic telescopes

* email:nk87@st-andrews.ac.uk

† Member of International Max Planck Research School for Astronomy and Cosmic Physics at the University of Heidelberg

‡ Royal Society University Research Fellow

1 INTRODUCTION

Gravitational microlensing (Paczynski 1986) occurs when the light from a source star is deflected by a massive compact object between the source and the observer, leading to an apparent brightening of the source, typically lasting a few days to a few weeks. When the deflecting body has multiple components, such as a planet orbiting its host star, there can be perturbations to the brightening pattern of observed sources. These perturbations can be large even when caused by low-mass objects, making them detectable using small ground-based telescopes. Modelling these lightcurve anomalies can lead to the detection of subtle effects, allowing for measurements of properties such as the source star limb-darkening coefficients (e.g. Cassan et al. 2004), the mass of stars with no visible companions (e.g. Ghosh et al. 2004), and the detection of extrasolar planets, as suggested by Mao & Paczynski (1991) and first achieved in 2003 (Bond et al. 2004).

Nevertheless, anomalous microlensing events usually require very detailed analysis for a full characterisation of their nature to be possible, making them challenging. This applies in particular to a class of microlensing events which display caustic crossing features in their lightcurves. These events are of primary interest, because they account for around ten percent of the overall number of detected microlenses, and they represent an important source of information on physical properties of binary stars (Jaroszynski et al. 2006). However there exist several degeneracies that affect the modelling of this type of events: without a robust modelling scheme and a full exploration of the parameter space, it is impossible to pin down the true nature of a given event. In addition to this, calculations of anomalous microlensing models for extended sources are very demanding computationally.

Given these issues, brute force is not an option when modelling caustic-crossing events, and one has to devise ways of speeding up calculations, for example by excluding regions of parameter space which cannot reproduce features that appear in data sets. A way to achieve this is to use a non-standard parameterisation of the binary-lens models that ties them directly to data features, as proposed by Cassan (2008), which we recall below.

In this paper, we present our method for exploring the parameter space, and describe our approach to find all possible models for a given event (Sec. 2). We then use OGLE-2007-BLG-472, a microlensing event observed in 2007 by the OGLE and PLANET collaborations, as an illustration of our methodology applied on a binary lens event which intrinsically harbors many ambiguities (Sec. 3). We finally discuss the implications of the individual competitive models that we find in order to discriminate between realistic microlensing scenarios.

2 BINARY-LENS EVENTS FITTING SCHEME

2.1 Parameterisation of binary lens lightcurves

A static binary lens is usually described by the mass ratio $q < 1$ of the two lens components and by their separation d , expressed in units of the angular Einstein radius (Einstein

1936),

$$\theta_E = \sqrt{\frac{4GM}{c^2} \left(\frac{D_S - D_L}{D_S D_L} \right)}, \quad (1)$$

where M is the mass of the lens, and D_L and D_S are the distances to the lens and the source respectively. Such a lens produces caustics where the magnification of the source diverges to infinity for a perfect point source. The positions, sizes and shapes of the caustics depend on d and q . For the binary lens case, caustics can exist in three different topologies, usually referred as *close*, *intermediate* and *wide*; bifurcation values between these topologies are analytical expressions relating d with q (Erdl & Schneider 1993). In the close regime, there are three caustics: a *central* caustic near the primary lens component, and two *secondary* caustics which lie off the axis passing through both lens components. In the intermediate case, there is only one large caustic on the axis. In the wide case, there is a *central* as well as a *secondary* caustic, both on the axis. The limits between these configurations are indicated as the dashed lines in e.g. Fig. 2 (see also Fig. 1 of Cassan (2008)).

The description of the lightcurve itself requires four more geometrical parameters in addition to d and q . In the current standard parameterisation of binary lens lightcurves, these are the source trajectory's angle α with the axis of symmetry of the lens, the time of closest source-lens approach to the binary lens centre-of-mass t_0 , the Einstein radius crossing time t_E and the source-lens separation at closest approach u_0 (in units of θ_E). Finally for a uniformly bright finite size source star, we add a further parameter, the source size ρ_* in units of θ_E . However, and as discussed in Cassan (2008), this parameterisation is not well adapted to conducting a full search of the parameter space, because the value of the parameters cannot be directly related to features present in the lightcurve, namely caustic crossings for the type of events we are discussing in this paper. Consequently, most of the probed models in a given fitting process do not exhibit the most obvious features in the lightcurve, leading to very inefficient modelling.

To avoid this drawback, Cassan (2008) introduced a new parameterisation in place of α, t_0, u_0 and t_E which is closely related to the appearance of caustic crossing features in the lightcurve. The caustic entry is then defined by a date t_{entry} when the source center crosses the caustic¹ and its corresponding (two-dimensional) coordinate ζ_{entry} on the source plane. However, since by definition this point is located on a caustic line, Cassan (2008) introduced a (one-dimensional) *curvilinear abscissa* s which locates the crossing point directly on the caustic, so that $\zeta_{\text{entry}} \equiv \zeta(s_{\text{entry}})$. A given caustic structure is fully parameterised by $0 \leq s \leq 2$. The caustic entry is then characterised by a pair of parameters $(t_{\text{entry}}, s_{\text{entry}})$, and in the same way the caustic exit by $(t_{\text{exit}}, s_{\text{exit}})$. These four parameters (in addition to d, q and ρ_*) which describe the caustic crossings therefore also define an alternative parameterisation of the binary lens, far better fitted to describing the problem at hand.

¹ Alternatively, any other point at a fixed position from the source center can be defined as a reference.

2.2 Exploration of the parameter space

We start by exploring a wide region of the parameter space with a (d, q) grid regularly sampled in logarithmic scale. This choice comes from the fact that the size of the caustic structures behave like power-laws of the lens separation and mass ratio, and so do the corresponding lightcurve anomalies. We fit for the remaining model parameters t_{entry} , t_{exit} , s_{entry} , s_{exit} and ρ_* , (d, q) being held fixed. From this, we then build a $\chi^2(d, q)$ map that we use to locate the best-fit (d, q) -regions. As mentioned previously, there exist binary lens configurations which involve central and secondary caustics. In these cases (*i.e.* in the wide and close binary cases) and following Cassan (2008), we study separately models where the source crosses the central or the secondary caustic by building two $\chi^2(d, q)$ maps, corresponding to each configuration.

In order to sample efficiently and extensively s_{entry} and s_{exit} (which determine the source trajectory), we use a genetic algorithm (e.g. Charbonneau 1995) that always keeps the best model from one generation to the next one (*elitism*). In fact, since we consider only models displaying caustics at the right positions, there are a couple of local minima associated with different $(s_{\text{entry}}, s_{\text{exit}})$ pairs which would usually be missed by other minimisation methods, while a genetic algorithm naturally solves this problem in an efficient way. However, since such an algorithm never converges exactly to the best model, we finally refine the model by performing a Markov-Chain Monte-Carlo (hereafter MCMC) fit: we start several chains and use the criterion by Geweke (1992) to assess convergence to a stationary posterior distribution of the parameter probability densities.

From the obtained χ^2 maps, we then identify all the local minima regions and use the corresponding best models found on the (d, q) grid as starting points to refine the parameters, including (d, q) that we now allow to vary. Since the fit is performed within a minimum χ^2 region, the fitting process is very stable and fast.

3 APPLICATION TO OGLE-2007-BLG-472

3.1 Alert and photometric follow-up

On 19 August 2007, the OGLE Early Warning System (Udalski 2003) flagged microlensing candidate event OGLE-2007-BLG-472 at right ascension $\alpha_{2000.0} = 17:57:04.34$, and declination $\delta_{2000.0} = -28:22:02.1$ or $l = 1.77^\circ$, $b = -1.87^\circ$.

The OGLE lightcurve has an instrumental baseline magnitude $I=16.00$, which may differ from the calibrated magnitude by as much as 0.5 magnitudes. Lensing by the star in the point source-point lens (hereafter PSPL) approximation accounts for a broad rise and fall in the lightcurve, peaking around $\text{MHJD}^2=4334.0$ with an apparent half-width at half-peak of about 10 days (Fig. 1). Although the observed OGLE flux rises only by 0.06 mag in the non-anomalous part of the lightcurve, the shape of the curve hints that blending is important for this target, with only $\sim 12\%$ of the baseline flux due to the un-magnified source.

On 19 August (MHJD=4331.5) an OGLE data point

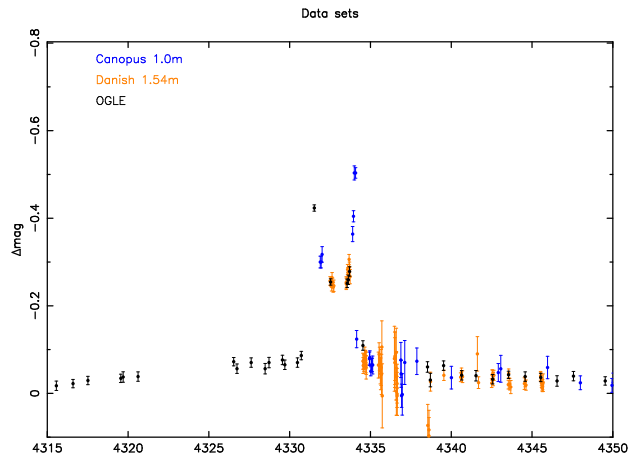


Figure 1. OGLE, UTas and Danish data set for OGLE-2007-BLG-472 data sets. Data points are plotted with $1\text{-}\sigma$ error bars. The x -axis is time in HJD-2450000.

Telescope	Data	Error bar rescaling factor
UTas 1.0m	34	1.79
Danish 1.54m	84	1.55
OGLE	857	1.21

Table 1. Datasets and error bar rescaling factors.

showed sudden brightening of the source, with subsequent PLANET (UTas Mt. Canopus 1.0m telescope in Tasmania and Danish 1.54m telescope at La Silla, Chile) and OGLE data indicating what appears to be a fold caustic crossing by the source, ending with a PLANET UTas data point on August 21 (MHJD=4334.1). The caustic entry is observed by a single OGLE point, while the caustic exit is well covered by our UTas data set (Fig. 1). Treating the lightcurve as the addition of an anomaly to a PSPL lightcurve, the underlying PSPL curve then apparently reaches peak magnification on August 22 (MHJD=4335.45). Particularly crucial in our data set is the UTas observation taken within a few hours of the caustic exit, which puts constraints on the position of the caustic exit on the lightcurve, and on the size of the source. Although some V-band observations were taken, the V lightcurve of this event is flat and does not allow us to place constraints on the V flux parameters.

3.2 Data reduction

We reduced the PLANET data for this event using the data reduction pipeline pysis3.0 (Albrow 2008). This pipeline uses a kernel as a discrete pixel array, as proposed by Bramich (2008), rather than a linear combination of basis functions. This has the advantage that it removes the need for the user to select basis functions manually, which can lead to problems if inappropriate functions are chosen. In addition to this, the pixel array kernel copes better with images that are not optimally aligned. The result of using this pipeline is a better reduction than was obtained with other methods. We kept all points with seeing <3.5 arcseconds. Although some dubious points remain with this simple cut, the size of their associated error bars reflects their lack of certainty

² MHJD=HJD-2450000

and ensures their weight in modelling procedures is appropriately reduced. Our final data set consists of 34 UTas data points, 84 points from the Danish 1.54m telescope, and 857 points from OGLE (Table 1).

3.3 Modelling OGLE-2007-BLG-472

After a first exploration of the parameter space, we find a best model (close to model C_c , see below) which we use as a basis to rescale our error bars. In fact, these can vary rather widely from one telescope to another and are often underestimated by photometry software. Ignoring this effect would misrepresent the relative importance of the data sets. From this step, we choose the rescaling factors shown in Table 1, obtained by setting $\chi^2/\text{d.o.f.} \simeq 1$ for each data set. We then use the rescaled data to perform a new parameter space exploration.

We then apply the fitting scheme detailed in section 2 to our data sets. In particular, we choose a spacing between the (d, q) grid points of 0.070 in $\log d$ and 0.275 in $\log q$. For the genetic algorithm fit, we use a model population of 200 individuals evolving during 40 generations, which has proven to be enough to safely locate the regions of minimum χ^2 . Finite source effects are computed using the adaptive contouring method of Dominik (2007).

The final $\chi^2(d, q)$ maps that we obtain are plotted in Fig. 2 for the intermediate and central caustic configurations, and Fig. 3 for the intermediate and secondary caustic. The red crosses show the underlying (d, q) grid, and the blue shaded contours indicate values of $\Delta\chi^2 = 5, 20, 50, 100, 250$, where the reference model is C_s , the global best-fitted model (as obtained in Section 3.5).

3.4 Excluding minima

Fig. 4 shows a zoom of this region (secondary caustic and close configuration $d < 1$), with an overplot of t_E isocontours (orange lines) roughly equally spaced on a logarithmic scale. With this fitting approach, we put no initial constraints on the Einstein time t_E , though it will always remain physical ($t_E > 0$). Since we are not using any Bayesian prior for this parameter, we find that very good fits to the data are obtained with values of $t_E > 300$ days, which correspond to the minimum region in the left lower part of Fig. 3. Such long Einstein times are not likely to happen commonly, and it may happen that some of the values found for t_0 correspond to a lightcurve that reaches its peak well in the future; these are very unlikely to be acceptable solutions. Hence, instead of using a *prior* for t_E in the fitting process, we adopt the *posterior* distribution of Dominik (2006), from which we see that $t_E > 400$ days, well in the tail of the distribution, can be used as a cut for a model to be physically plausible. Thus in the following, we will not consider solutions with values of t_E greater than 400 days. This means that we will not include the low- q ($q \sim 0.001$) minima in the following discussion.

Although a very well-covered lightcurve generally enables a good characterisation of the deviation caused by the caustic approach or crossing, degeneracies make finding a unique best-fitting model difficult. In particular, Griest & Safizadeh (1998) and Dominik (1999) identified a two-fold degeneracy in the projected lens components separation parameter d , under the change $d \leftrightarrow 1/d$, when

$q \ll 1$. Moreover, Kubas et al. (2005) showed that very similar lightcurves could arise for a source crossing the secondary caustic of a wide binary system and for the central caustic of a close binary system. These degeneracies cause widely separated χ^2 minima in the parameter space, which must then be located by exploring the parameter space thoroughly. In addition to these degeneracies, imperfect sampling can increase the number of local χ^2 minima; short event in particular are prone to under-sampling, leading to difficulties in modelling. OGLE-2007-BLG-472 is no exception, as shown in the next section.

3.5 Refining local minima

We see from Fig. 2 (intermediate and central caustic) that there are three broad local minima in the region around the white filled circles marked as C_c , I and W_c (“I”, “C” and “W” for intermediate, close and wide models respectively, and subscript “c” for central caustic). In Fig. 3 (intermediate and secondary caustic), a best-fit region can easily be located around the region marked C_s (subscript “s” for secondary caustic), besides region I .

Now allowing for the parameters d and q to vary as well, we use our MCMC algorithm to find the best solutions in each of these local minimum regions. These are identified with white filled circles on Fig. 2 and 3 and correspond to the models listed in Table 2, and shown in Fig. 5, 6, 7 and 8. The best model lightcurve is dominated by strong caustics, which all viable models must reproduce, with the low-magnification base PSPL curve barely noticeable. All models have the first anomalous OGLE points on the descending side of the caustic entry except for the worst model, model W_c , which has this OGLE point on the ascending part of the caustic entry. Statistically, the former case is more likely to be observed since the ascending part of the caustic entry happens much more rapidly than the descending side.

Our best model, C_s , has $\chi^2 = 949$ for 975 data points, with the other competitive models at $\Delta\chi^2 = 13.2$ (model C_c), $\Delta\chi^2 = 23.5$ (model I) and $\Delta\chi^2 = 39.6$ (model W_c).

3.6 Discussion

Fig. 4 shows that the models with a source crossing a secondary caustic have increasingly large values of t_E as they go towards lower values of the mass ratio. This is expected since the time Δt between t_{entry} and t_{exit} is fixed by the data. As the size of caustics scales with $q^{1/2}$, and $t_E \sim \Delta t/q^{1/2}$, the source must therefore cross the Einstein Ring over a longer timescale in order to conserve the right timing for s_{entry} and s_{exit} . In addition to this, blending decreases for decreasing values of q , and therefore decreases with increasing t_E , contrary to what might be expected. Indeed, one would expect the blending factor $g = F_B/F_S$ (where F_B and F_S are the blend and source flux respectively) to increase with increasing t_E in order to mask long timescales and reproduce the observed timescale. However in this region of parameter space, the caustics are weak, which means that too much blending would not allow models to reproduce the observed rise in the source magnitude at the caustic entry and caustic exit. For a region of parameter space to contain satisfactory models, there must therefore be a fine balance between blending, timescale and mass ratio.

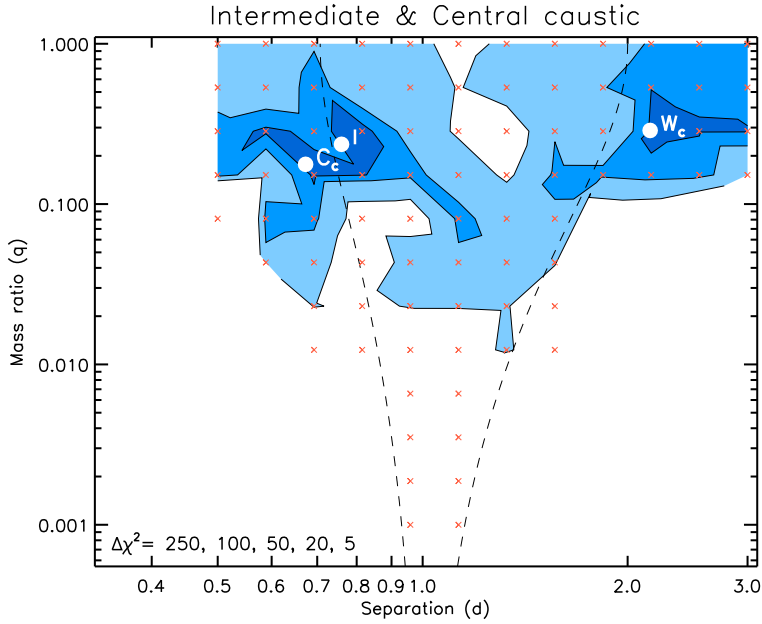


Figure 2. $\chi^2(d, q)$ map for the intermediate and central caustic configurations. Contour lines and minima regions (in blue shades) are plotted at $\Delta\chi^2 = 5, 20, 50, 100, 250$. The two dashed curves are the separation between the close, intermediate and wide regimes. The models are labelled and marked with white filled circles.

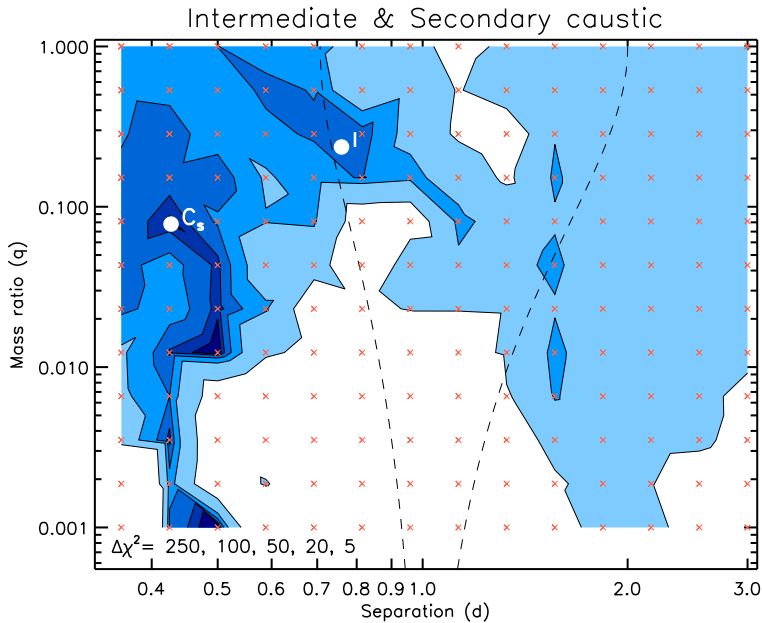


Figure 3. Same as Fig. 2 for the the intermediate and secondary caustic configuration.

For models where the source crosses a central caustic, the impact parameter u_0 must decrease with decreasing mass ratio, since the size of central caustic decreases with decreasing mass ratio, and the range of allowed u_0 decreases if the source must cross the caustic. This means that for

smaller mass ratios, blending will have to increase in order to mask the correspondingly higher PSPL magnification of the source that results from the smaller impact parameter.

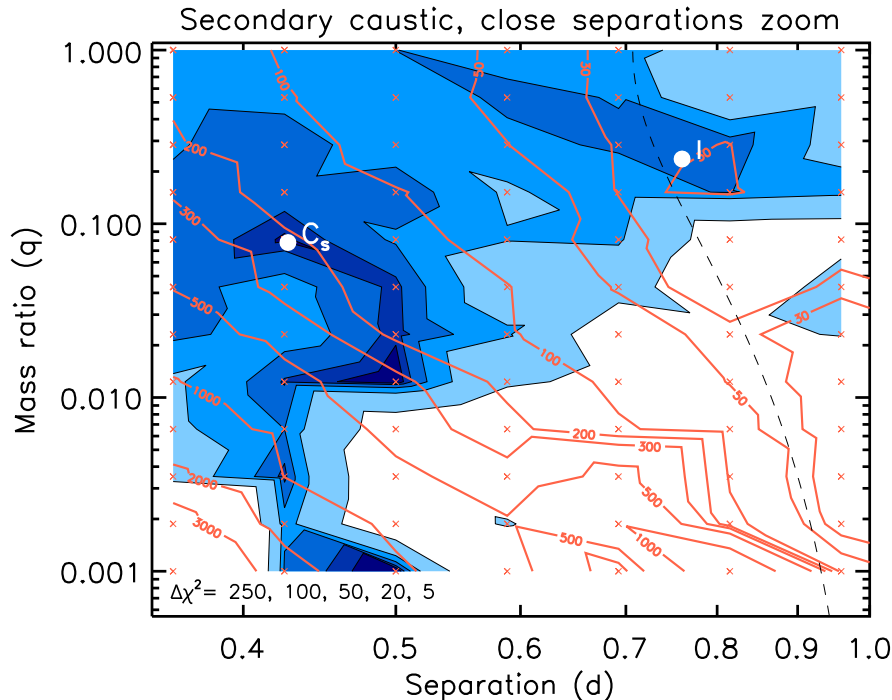


Figure 4. Map of the value of t_E in the (d, q) plane for converged models at each grid point, superimposed on the χ^2 map, zoomed in on the close regime part of parameter space. Contours lines (orange) are labeled with their corresponding value of t_E while χ^2 contour lines are plotted at $\Delta\chi^2 = 5, 20, 50, 100, 250$ and filled with gradual shades of blue. The dashed curve is the separation between the close and intermediate regimes. The models of Table 2 are labelled and marked with white filled circles.

3.7 Physical properties of the models

3.7.1 Source characteristics

A colour-magnitude diagram of the field (Fig. 9) was produced extracting 1497 stars from I and V images at $t = 4340.08$ (I) and $t = 4340.13$ (V) taken at the Danish 1.54m telescope. The combination of the source and the blend lies very slightly blueward of the red giant clump, at $(V - I) = 2.43$. All the models, however, are heavily blended (Table 2). The actual source magnitude and blending magnitude for each model can be found using the equations $I_s = I_{\text{base}} + 2.5 \log(1 + g)$ and $I_b = I_s - 2.5 \log(g)$.

Using this equation, we find source magnitudes ranging from 17.89 (model C_s) to 20.21 (model C_c) (see Table 2). Our V-band data set does not allow us to determine the source’s colour, but assuming that the source is a main sequence star we use the calculated I magnitude of the source for each model to estimate a colour, using the results of Holtzman et al. (1998). This then enables us to estimate the source’s angular radius which we use in Section 3.7.2 to compute probability densities of the lensing system’s properties.

We calibrate the baseline magnitude of our target (source and blend combined) using the location of the red clump as a reference. We find $I_{\text{base}} = 15.61 \pm 0.10$, which is in agreement with the OGLE value of $I_{\text{base}} = 16.00 \pm 0.50$. Comparing this to the location of the red clump, we can derive an estimate for the reddening coefficient A_I . From Hipparcos results, Stanek & Garnavich (1998) find an absolute magnitude for the red clump at $M_{I,RC} = -0.23 \pm 0.03$. Using

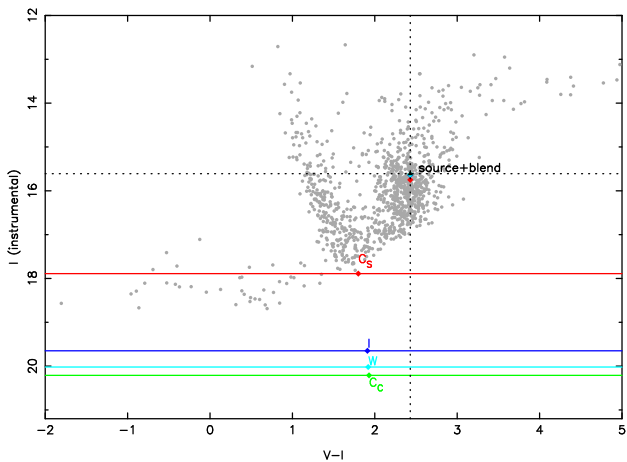


Figure 9. Colour - Magnitude diagram of the field. The target OGLE-2007-BLG-472 is shown as a black triangle at $(V - I, I) = (2.43, 15.61)$. The position of the deblended source for each model is labeled and indicated by a dotted line and a coloured diamond, with the blend for each model also plotted as a diamond in the same colour.

a distance modulus to the galactic centre of $\mu = 14.41 \pm 0.09$ (i.e. assuming $D_S = 7.6$ kpc) (Eisenhauer et al. 2005), this translates to a dereddened magnitude for this target of $I_{\text{base}} = 14.18 \pm 0.09$. Hence using the relation $A_I = I_{\text{base}} - M_{I,RC} - \mu$, we get a value for the I-band reddening parameter of $A_I = 1.43 \pm 0.13$. Alternatively, fitting 2MASS

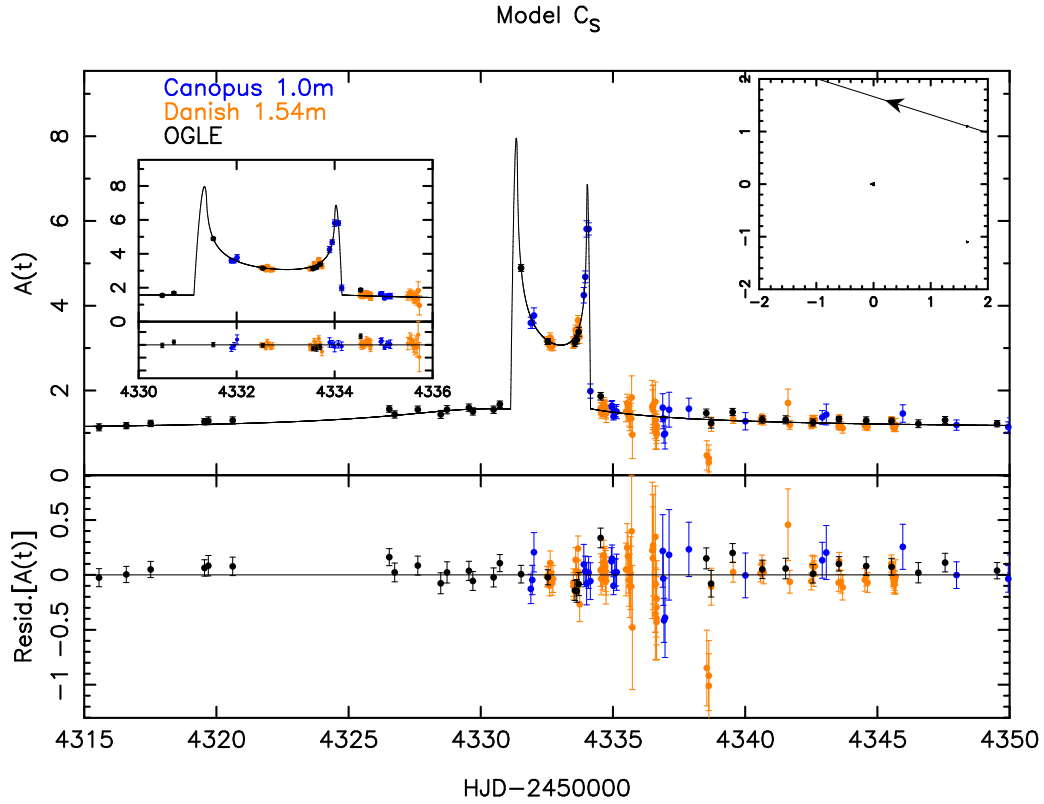


Figure 5. Best-fitting binary lens model C_s with residuals and a zoom on the anomaly (left inset). Data points are plotted with $1\text{-}\sigma$ error bars. The trajectory of the source in the lens plane with the caustics is plotted as an inset in the top right corner of the figure, with the primary lens component located at the coordinate system's origin.

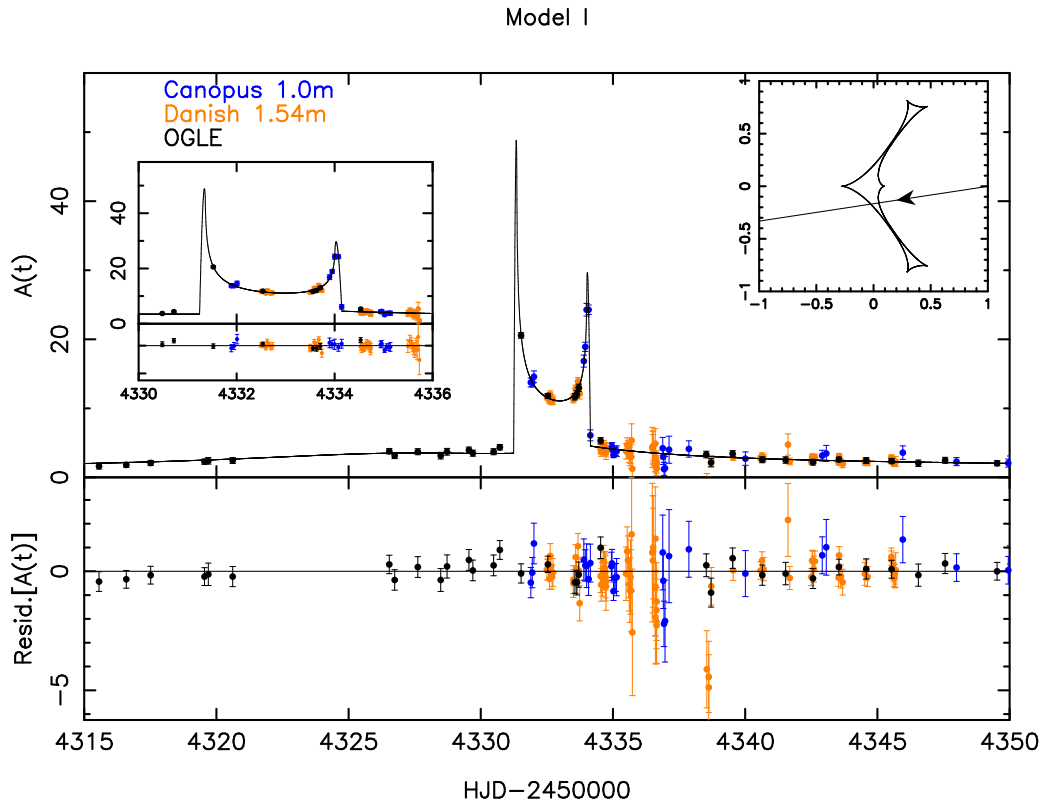


Figure 6. Same as Fig. 5 for model I .

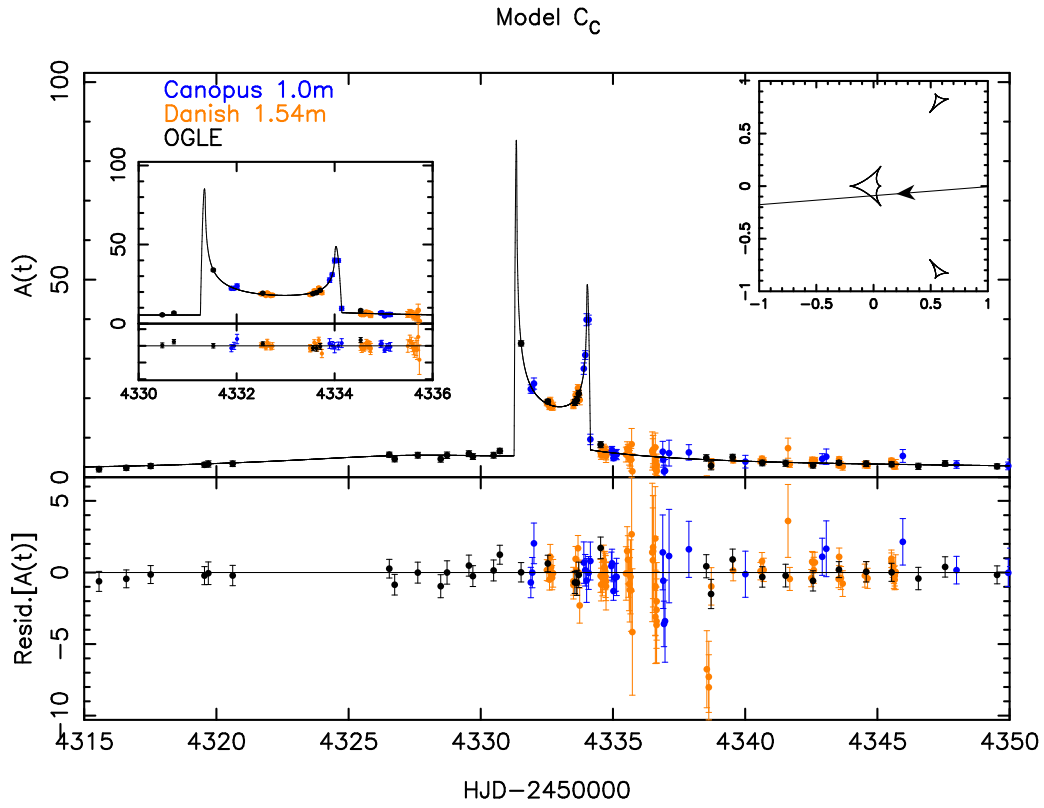


Figure 7. Same as Fig. 5 for model C_c .

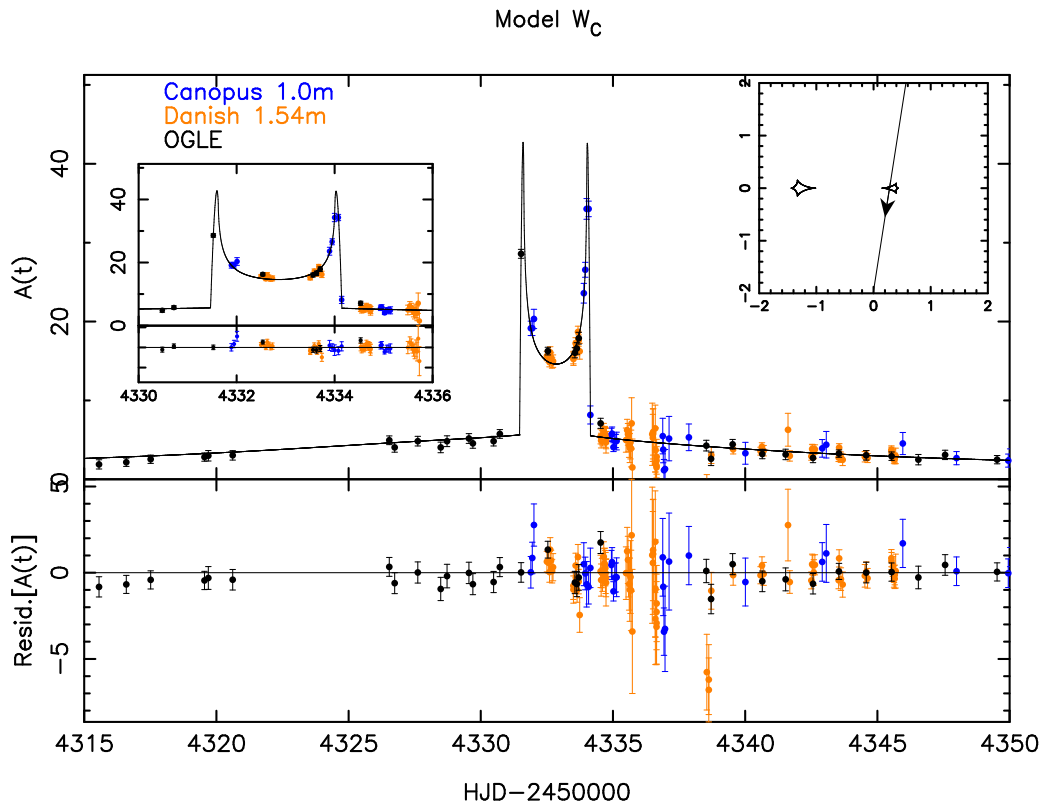


Figure 8. Same as Fig. 5 for model W_c .

Table 2. Best-fitting binary lens model parameters. The blending factor $g(I) = F_B(I)/F_S(I)$ is given for the OGLE data (I -band). The error bars were rescaled for each telescope by the factor given in Table 1, which lead to the rescaled χ^2 indicated here. Physical parameters are also given for each model, for the case of a lens in the disk, and a lens in the bulge. These were calculated using the procedure detailed in Sec. 3.7.2

Parameter	Model C_s	Model C_c	Model I	Model W_c	Units
χ^2 (rescaled σ)	949.00	963.16	972.48	988.55	—
$\Delta\chi^2$	—	13.2	23.5	39.8	—
χ_{UTas}^2	23.79	24.83	26.41	28.86	—
χ_{Danish}^2	79.77	79.60	80.75	88.93	—
χ_{OGLE}^2	845.50	858.77	865.24	870.55	—
t_0	4587.18 ± 0.80	4332.27 ± 0.29	4332.10 ± 0.27	4334.99 ± 0.28	MHJD
t_E	213.82 ± 1.04	52.00 ± 3.63	38.32 ± 2.60	53.46 ± 0.81	days
α	2.810 ± 0.006	3.227 ± 0.030	3.305 ± 0.037	4.570 ± 0.018	rad
u_0	-1.573 ± 0.013	0.091 ± 0.005	0.164 ± 0.019	0.277 ± 0.010	—
$\rho_*/10^{-3}$	0.34 ± 0.01	0.98 ± 0.19	1.55 ± 0.16	1.33 ± 0.05	—
d	0.427 ± 0.002	0.673 ± 0.011	0.760 ± 0.015	2.158 ± 0.0169	—
q	0.078 ± 0.001	0.177 ± 0.017	0.236 ± 0.024	0.288 ± 0.0096	—
$g(I) = F_B(I)/F_S(I)$	7.15 ± 0.013	68.11 ± 0.013	40.13 ± 0.09	56.98 ± 0.019	—
I_s	17.89 ± 0.01	20.21 ± 0.01	19.65 ± 0.09	20.02 ± 0.01	—
I_b	15.75 ± 0.01	15.63 ± 0.01	15.64 ± 0.09	15.63 ± 0.01	—
$(V - I)_s$	1.80 ± 0.10	1.93 ± 0.11	1.91 ± 0.11	1.92 ± 0.12	—
θ_*	1.18 ± 0.24	0.46 ± 0.09	0.59 ± 0.12	0.50 ± 0.10	μas
<hr/>					
Lens in the Disk					
M_1	$1.50^{+1.85}_{-0.58}$	$0.42^{+0.40}_{-0.22}$	$0.34^{+0.36}_{-0.18}$	$0.34^{+0.37}_{-0.18}$	M_\odot
M_2	$0.12^{+0.14}_{-0.05}$	$0.07^{+0.07}_{-0.04}$	$0.08^{+0.08}_{-0.04}$	$0.10^{+0.11}_{-0.05}$	M_\odot
D_L	$1.00^{+0.95}_{-0.36}$	$5.7^{+1.1}_{-1.5}$	$6.1^{+1.1}_{-1.5}$	$6.1^{+1.0}_{-1.5}$	kpc
v	25^{+24}_{-9}	80^{+15}_{-21}	93^{+16}_{-22}	67^{+11}_{-16}	km s^{-1}
<hr/>					
Lens in the Bulge					
M_1	41^{+14}_{-14}	$1.25^{+1.47}_{-0.59}$	$0.79^{+0.93}_{-0.35}$	$0.79^{+0.94}_{-0.36}$	M_\odot
M_2	$3.2^{+1.1}_{-1.1}$	$0.22^{+0.26}_{-0.10}$	$0.19^{+0.22}_{-0.08}$	$0.23^{+0.27}_{-0.10}$	M_\odot
D_L	$6.7^{+0.4}_{-0.7}$	$7.3^{+0.6}_{-0.8}$	$7.3^{+0.6}_{-0.8}$	$7.3^{+0.6}_{-0.8}$	kpc
v	167^{+10}_{-17}	102^{+8}_{-12}	111^{+10}_{-12}	79^{+6}_{-8}	km s^{-1}

isochrones to our CMD, we obtain a value $A_I = 1.46 \pm 0.08$ and $E(V - I) = 1.46 \pm 0.11$. We use these values of reddening to determine dereddened magnitudes and colours for the source of each model. These, together with the surface brightness relations from Kervella & Fouqué (2008), allow us to calculate the apparent angular radius of the source θ_* for each of the models, given in Table 2.

3.7.2 Lens characteristics

Although the characteristics of any microlensing event depend on various properties of the lensing system, including the mass of the lenses, the only measurable quantity that can be directly related to physical properties of the lens is the timescale of the event t_E . While the physical properties of the lensing system can be fully constrained when the photometry is affected by both finite source-size effects and par-

allax, when these are not measured, such as is the case with our analysis OGLE-2007-BLG-472, we can still use Bayesian inference to determine probability densities of physical properties of the lens, based on a chosen Galactic model. We have chosen not to include parallax in our analysis because its effect would be very small for such a low-magnification event; in addition to this, we are only seeking a first-order analysis of binary-lens events with our current method, although second-order effects such as parallax and lens rotation will be taken into account in future work.

We use our fitted value of the source size parameter ρ_* to place constraints on the mass of the lens, which can be expressed as a function of fractional distance $x = D_L/D_S$ and the source size ρ_* as (e.g. Dominik 1998)

$$\frac{M(x)}{M_\odot} = \frac{c^2}{4GM_\odot} \frac{D_S \theta_*^2}{\rho_*^2} \frac{x}{1-x}, \quad (2)$$

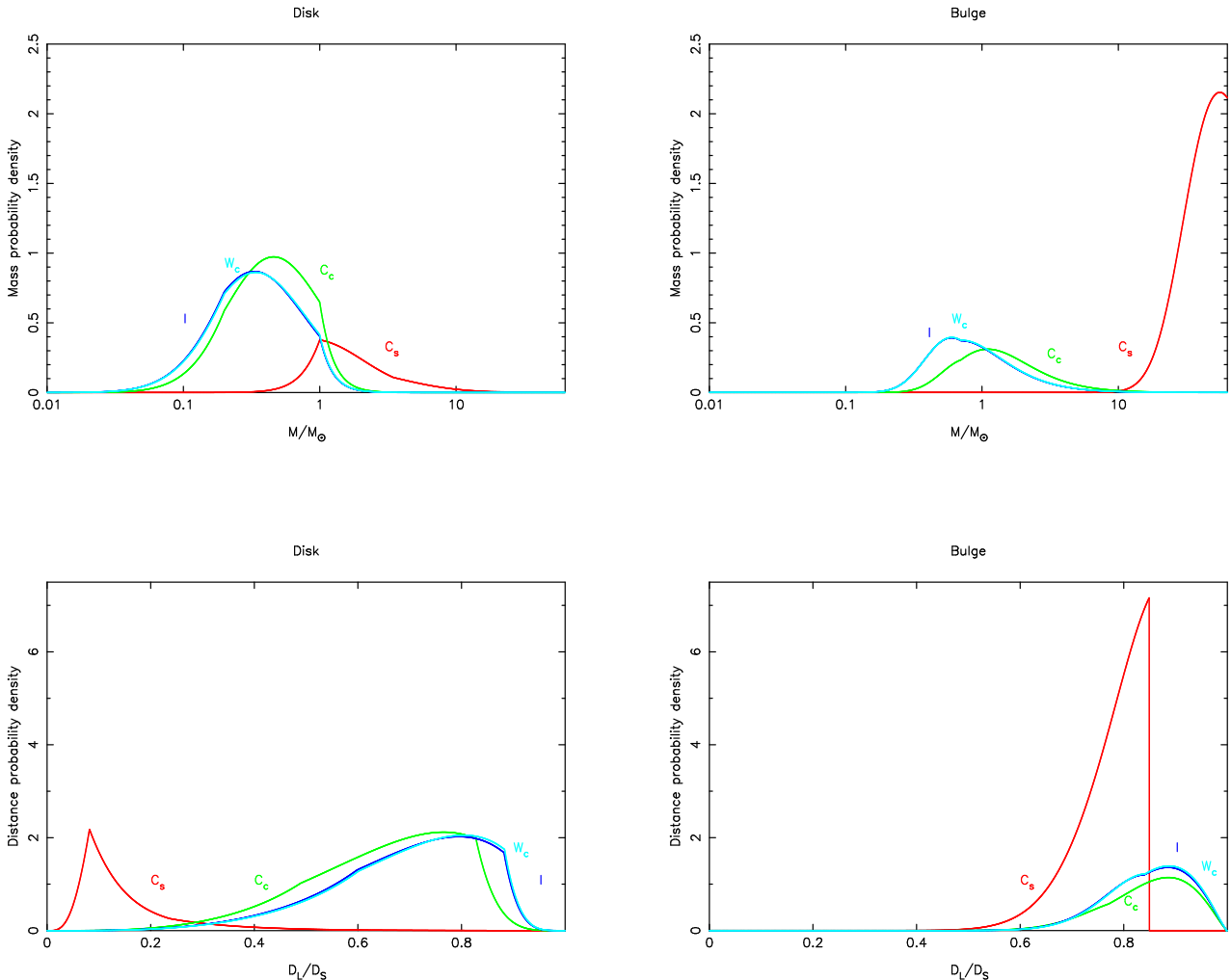


Figure 10. Probability densities for the mass of the primary lens star and the fractional distance D_L/D_S , for a lens in the disk (left side) and a lens in the bulge (right side). The values quoted in Tables 2 & 2 are the median value and the limits of the 68.3% confidence interval. On each plot, the probability densities are plotted for model C_s (red), model C_c (green), model I (dark blue), and model W_c (light blue).

where M is the mass of the lens, θ_* is the angular radius of the source, the value of which is given in Table 2, and other quantities are defined as before. The mass-distance curve showing constraints from this equation is plotted on Fig. 11.

However, since we cannot measure parallax for this event, we use a probabilistic approach following that of Dominik (2006) to derive probability densities for physical properties of lens components. The Galactic model used here is a piecewise mass spectrum (e.g. Chabrier 2003), two double exponentials for the disk mass density and a barred bulge tilted at an angle of 20° with the direction to the Galactic centre (Dwek et al. 1995), and the distribution of effective transverse velocities used in Dominik (2006).

Using these galactic models, we infer properties for the lensing system, separating the cases where the lens is in the Galactic disk and in the Galactic bulge. For a lens in the disk, we find a primary mass $1.50^{+1.85}_{-0.58} M_\odot$ and a secondary mass of $0.12^{+0.14}_{-0.05} M_\odot$, at a distance of $1.00^{+0.95}_{-0.36}$ kpc with a lens velocity of 25^{+24}_{-9} km s $^{-1}$. For a lens in the bulge, we find a primary mass $41^{+14}_{-14} M_\odot$ and a secondary mass of

$3.2^{+1.1}_{-1.1} M_\odot$, at a distance of $6.7^{+0.4}_{-0.7}$ kpc with a lens velocity 167^{+10}_{-17} km s $^{-1}$. These are the physical lens properties for the lowest- χ^2 model (model C_s). The values of these physical parameters for the other models are given in Table 2. Probability densities of these properties for all models are plotted on Fig. 10.

3.7.3 Discussion

For our lowest- χ^2 model, the parameters we find imply very unusual properties of the lensing system. As discussed in Sec. 3.4, the fact that we find these types of models is a consequence of the fitting approach we are taking. Traditional fitting methods would struggle to find these minima, since most of them require providing a starting point in parameter space. This is an issue when solely using an MCMC algorithm to fit microlensing events: although an MCMC run may be able to make its way through parameter space to find minima reasonably far away from its starting point, it is highly unlikely that a chain will be able to reach a minimum that has parameters different from the starting point

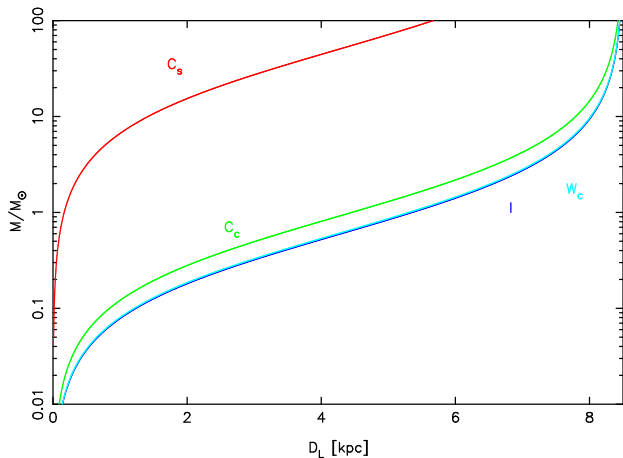


Figure 11. Mass-distance diagram showing the constraint on the lens mass from the source size, given by Eq. (2), for each model. The curves are labeled with the name of the model to which they correspond.

by more than one order of magnitude. As we see from Fig. 4, there exist minima in many parts of parameter space, with values of t_E that are different by almost two orders of magnitude. These parameters are non-intuitive, since they cannot be guessed only by looking at the lightcurve. As a result, it is improbable that this kind of parameters will be used as starting points for "classic" fitting algorithms.

We solve this problem for the static binary-lens case by resorting to the method described in Sec. 2.2. Using this approach, we manage to systematically locate minima in parameter space. However, one then has to be careful with interpreting the significance of the obtained model parameters. The shape of probability densities shown in Fig. 10 for model C_s indicates that our value of t_E push the lens mass towards the end of the adopted mass spectrum in the Galactic model we have adopted. This results in the abrupt transients seen on Fig. 10. Similarly, the mass-distance curve for model C_s on Fig. 11 shows that the mass of the lens increases very rapidly for lenses above ~ 1 kpc. These unusual curves are caused by a value of $t_E \sim 200$ days. Models with $t_E \sim 3000$ days (corresponding to the low- q minimum visible on Fig. 3 & 4) are obviously not acceptable, but how can we formally reject them? Finding these models from minima in the χ^2 surface shows the limits of using χ^2 as a strong criterion for favouring models. A solution to this would be to use prior distributions on as many of the parameters as we can. During the MCMC part of our fitting process, this would mean that we obtain posterior distributions that are different from the ones obtained without using prior distributions on the parameters, or, equivalently, assuming uniform priors for all parameters. Such priors can be obtained in various ways, such as looking at the distribution of timescales for past microlensing events or calculating these distributions from Galactic models (e.g. Dominik 2006), or by using luminosity functions of the Galactic bulge to find a prior for the blending factor g (e.g. Holtzman et al. 1998). Such work requires careful consideration of which priors are most appropriate to use, and is beyond the scope of this paper. Using these priors in combination with our method to find minima will lead to more robust determination of minima

by taking into account our knowledge of physical parameter distributions.

4 SUMMARY AND PROSPECTS

Our analysis of OGLE-2007-BLG-472 is a good illustration of the importance and power of using parameters that are related to actual observed features. Indeed, despite incomplete coverage of the caustic entry and high blending, a few crucial data points and an appropriate choice of non-standard parameters enable us to find several good binary-lens model fits to our data for this event by exploring the parameter space systematically. Some of the good fits that we identify have unphysical parameters, and we must then reject them. However using this parameterisation allows us to be certain that the parameter space has been thoroughly explored. We find four models with different parameters: two close binary models, one intermediate configuration, and a wide binary model. The lowest- χ^2 model corresponds to a G dwarf star being lensed by a binary system with component masses $1.50^{+1.85}_{-0.58} M_\odot$ (for the primary) and $0.12^{+0.14}_{-0.05} M_\odot$ (for the secondary), which are compatible with our blending values. However it is obvious from physical parameter distributions that using χ^2 as a sole criterion for determining the best model is insufficient, because it does not take into account our knowledge of the distributions of physical parameters.

Since the approach presented in this paper can form the basis for a systematic, wide ranging exploration of the parameter space to localise all possible models for a given data set, it is particularly relevant to current efforts to automatise real-time fitting of binary-lens events. This could prove useful to provide faster feedback on the events being observed and prioritise observing schedules, especially on robotic telescopes. Expanding robotic telescope networks controlled by automated intelligent algorithms are expected to play an increasingly important role in microlensing surveys in the coming years (e.g. Tsapras et al. 2008). Fitting methods such as the one described in this paper are essential for making sure any anomalies are interpreted correctly, and that minima are located in as large a part of parameter space as possible.

ACKNOWLEDGEMENTS

NK acknowledges STFC studentship PA/S/S/2006/04497 and an STFC travel grant covering his observing run at La Silla. We thank David Warren for financial support for the Mt Canopus Observatory. NK thanks Pascal Fouqué for organising a workshop in Toulouse in November 2007, and Joachim Wambsgans and Arnaud Cassan for their invitation to visit the Astronomisches Rechen-Institut in Heidelberg in April 2008. We would like to thank the anonymous referee for his helpful comments on the manuscript. We also thank the University of Tasmania for access to their TPAC supercomputer on which part of the calculations were carried out. PF expresses his gratitude to ESO for a two months invitation at Santiago headquarters, Chile in October and November 2008. The OGLE project is partially supported by the Polish MNiSW grant N20303032/4275.

References

- Bond I. A., et al., 2004, *ApJ*, 606, L155
Bramich D. M., 2008, *MNRAS*, 386, L77
Cassan A., 2008, *A&A*, 491, 587
Cassan A., et al., 2004, *A&A*, 419, L1
Chabrier G., 2003, *PASP*, 115, 763
Charbonneau P., 1995, *ApJS*, 101, 309
Dominik M., 1998, *A&A*, 330, 963
—, 1999, *A&A*, 349, 108
—, 2006, *MNRAS*, 367, 669
—, 2007, *MNRAS*, 377, 1679
Dwek E., et al., 1995, *ApJ*, 445, 716
Einstein A., 1936, *Science*, 84, 506
Eisenhauer F., et al., 2005, *ApJ*, 628, 246
Erdl H., Schneider P., 1993, *A&A*, 268, 453
Geweke J., 1992, *Evaluating the Accuracy of Sampling-Based Approaches to the Calculation of Posterior Moments*. Oxford University Press, pp. 169–193
Ghosh H., et al., 2004, *ApJ*, 615, 450
Griest K., Safizadeh N., 1998, *ApJ*, 500, 37
Holtzman J. A., Watson A. M., Baum W. A., Grillmair C. J., Groth E. J., Light R. M., Lynds R., O’Neil Jr. E. J., 1998, *AJ*, 115, 1946
Jaroszynski M., et al., 2006, *Acta Astronomica*, 56, 307
Kervella P., Fouqué P., 2008, *A&A*, 491, 855
Kubas D., et al., 2005, *A&A*, 435, 941
Mao S., Paczyński B., 1991, *ApJ*, 374, L37
Paczynski B., 1986, *ApJ*, 304, 1
Stanek K. Z., Garnavich P. M., 1998, *ApJ*, 503, L131+
Tsapras Y., et al., 2008, *ArXiv e-prints*, 808
Udalski A., 2003, *Acta Astronomica*, 53, 291

This paper has been typeset from a $\text{\TeX}/\text{\LaTeX}$ file prepared by the author.